Physics-Guided Transfer Learning of Soil Freezing Characteristic Parameterization for Coupled Thermo-Hydro-Chemical Simulation of Saline Permafrost

Xueyang Wang and Ming Xiao

Department of Civil and Environmental Engineering
The Pennsylvania State University, University Park, PA 16802, USA

Journal submission

This manuscript has been submitted to the *Journal of Geotechnical and Geoenvironmental Engineering* (ASCE) and is currently under review.

Corresponding author

Xueyang Wang: xxw5360@psu.edu

Coauthor contact

Ming Xiao: mzx102@psu.edu

PHYSICS-GUIDED TRANSFER LEARNING OF SOIL FREEZING CHARACTERISTIC PARAMETERIZATION FOR COUPLED THERMO-HYDRO-CHEMICAL SIMULATION OF SALINE PERMAFROST

XUEYANG WANG AND MING XIAO

Abstract. Coupled thermal–hydraulic–chemical (THC) simulation is an important tool for predicting thaw, liquid-water redistribution, and solute transport in saline permafrost. A major challenge is to determine the constitutive parameters that control coupled THC processes, especially because soil freezing characteristic (SFC) measurements for saline, organic-rich soils are limited. This study develops a physics-guided transfer learning (PG-TL) framework for SFC parameterization and integrates the parameterization into a THC simulation framework. The generalized Clapeyron equation–van Genuchten (GCE–VG) relation serves as a physics-informed constraint by expressing unfrozen water content (UWC) as a constitutive function of matric potential, temperature, and solute concentration. Within the transfer learning framework, a pedotransfer function (PTF) maps soil index properties to VG parameters. The PTF is pre-trained on a soil water characteristic (SWC) database and then adapted to a smaller SFC database containing saline and organic soil samples. The PG-TL-based SFC parameterization is further implemented in a one-dimensional (1D) finite-volume THC simulator. The simulator is calibrated against borehole temperature observations and active layer thickness records for a saline permafrost profile near Utqiaġvik, Alaska. Scenario simulations are conducted to examine the effects of seawater intrusion and surface organic-layer degradation on thaw-front development. By the third simulation year, the annual maximum thaw depth increased by 6.8%, 27.3%, and 34.3% relative to the undisturbed baseline under seawater intrusion, organic-layer degradation, and their combined disturbance, respectively. The proposed framework provides a solver-compatible constitutive parameterization for saline permafrost assessment and supports coupled THC analysis where direct freezing measurements are sparse.

1. Introduction

Predicting thaw and liquid-water redistribution in permafrost requires resolving coupled thermal, hydraulic, and geochemical processes that vary strongly over short spatial distances. In ice-rich and saline permafrost terrain, surface conditions such as ice-wedge polygons, thermokarst, surface ponding, and infrastructure disturbance can change over meters to tens of meters, while subsurface texture, ice content, salinity, and organic matter may vary over vertical intervals of only a few tens of centimeters (Kokelj and Jorgenson 2013; Liljedahl et al. 2016; Shur and Jorgenson 2007; Walvoord and Kurylyk 2016). Such subsurface heterogeneity affects the latent

Key words and phrases. Soil freezing characteristic curve; Saline permafrost; Thermo-hydro-chemical modeling; Transfer learning; van Genuchten parameters.

Corresponding author: Xueyang Wang (xxw5360@psu.edu).

heat effects, hydraulic conductivity, liquid-water migration, and solute mobility, which thereby governs thaw progression, differential ground subsidence, and carbon and contaminant release.

The soil freezing characteristic (SFC) describes the equilibrium between UWC and subzero temperature and provides a key constitutive basis for permafrost hydrothermal modeling. A common SFC formulation combines the generalized Clapeyron equation (GCE) with the van Genuchten (VG) water-retention model (Dall'Amico et al. 2011; Kurylyk and Watanabe 2013; Zhang et al. 2024). The GCE converts temperature depression into an equivalent matric potential of unfrozen pore water. The VG model then converts the equivalent matric potential into UWC. The classic GCE-VG model mainly represents capillary-controlled freezing. However, frozen soils are also influenced by texture, salinity, and soil organic matter (SOM). The key VG parameters include saturated water contents θ_s, residual water content θ_r, the inverse of air-entry suction α, and the pore-size distribution index n, respectively (van Genuchten 1980). Texture controls pore-size distribution and therefore influences α, n, and the overall shape of the SFC curve (Benson et al. 2014). High specific surface area of fine-grain soil increases adsorbed water and contributes to residual unfrozen water (Anderson and Tice 1973; Wang and Lu 2026). Salinity lowers the chemical potential of pore water and depresses the equilibrium freezing temperature (Amankwah et al. 2021; Zhou et al. 2020). During freezing, solutes are excluded from ice and become concentrated in the remaining liquid. This process further reshapes the SFC. Organic-rich soils commonly have high porosity, which can increase θ_s. SOM also increases specific surface area and adsorptive water, thereby increasing residual unfrozen water (Chuvilin et al. 2022; Watanabe and Wake 2009). These soil properties interact through pore-size distribution, interfacial water retention, osmotic potential, and pore-structure deformation. The coupling effects on GCE-VG parameters can be nonlinear and dependent, which limits the reliability of empirical VG parameter assignment for heterogeneous saline permafrost with varying organic content.

Machine-learning methods, including artificial neural networks (ANN), random forests, and extreme gradient boosting models, have been applied to predict UWC and estimate SFC curves from basic soil index properties (Bi et al. 2023; Kim et al. 2025; Li and He 2024; Park et al. 2025; Ren et al. 2023). The approaches generally provide accurate pointwise UWC estimates at prescribed temperatures. Recent work by Liu et al. (2026) advanced these methods by embedding an ANN-based UWC model into a thermo-hydraulic simulation and validating it against laboratory experiments. In the model, however, the ANN returns UWC from soil temperature, while hydraulic conductivity comes separately from an empirically parameterized VG model. Black-box models such as ANNs require large training sets to generalize, yet SFC measurements from undisturbed permafrost cores remain scarce, particularly for saline and

organic-rich soils (Chuvilin et al. 2022). This data limitation leaves the effects of soil organic matter and salinity insufficiently constrained in SFC parameterization.

The limited availability of SFC data can be partly addressed by using the more abundant soil water characteristic (SWC) measurements. This strategy relies on the thermodynamic analogy between soil drying and soil freezing (Black and Tice 1989; Koopmans and Miller 1966). Under phase equilibrium, the generalized Clapeyron equation links matric potential in the drying domain to temperature depression in the freezing domain (Dall'Amico et al. 2011; Kurylyk and Watanabe 2013). The drying-freezing analogy allows SWC-derived retention behavior to provide physically informed constraints on SFC parameterization. Because SWC measurements for organic samples are more abundant than SFC measurements, they can serve as useful auxiliary information for estimating GCE–VG parameters (Zhou et al. 2018). However, the drying-freezing analogy is not exact. The SWC and SFC involve different interfaces (air–water versus ice–water), and their interfacial tensions produce systematic deviations whose magnitude depends on soil type and the balance between capillary and adsorptive forces (Koopmans and Miller 1966; Wang and Hu 2023). These differences motivate the use of transfer learning to adapt SWC-informed constraints to freezing-domain behavior.

The key contribution of this study is to establish a pedotransfer function (PTF) for SFC parameterization and coupled THC simulation workflow for saline and organic permafrost, with three innovations:

- A physics-guided transfer learning framework is developed to estimate VG parameters from soil index properties, linking UWC with temperature, pore pressure, salinity, and soil composition in saline and organic-rich frozen soils.
- Soil property information and long-term meteorological and field observations are incorporated into the THC modeling framework, to enable site-specific representation of coupled water–salt–heat dynamics in saline permafrost.
- Simulation of a monitored saline permafrost profile near Utqiaġvik, Alaska is used to quantify how salt intrusion and organic-layer disturbance affect water–salt–heat redistribution and thaw development. This application provides a quantitative approach and process-level insight for evaluating environmental risks in saline Arctic settings.

This paper is organized as follows. The physics-guided transfer learning framework for SFC parameterization is first introduced, including the physical formulation, transfer learning strategy, and model calibration and training protocol. The governing equations for the THC simulation are then presented, together with the boundary conditions and numerical implementation. The data sources and model inputs are described next, including the SFC dataset compilation

and the climate forcing and ground conditions used in the THC simulations. The results and discussion then evaluate the PG-TL-based SFC prediction and demonstrate its application to coupled THC simulations. Finally, the limitations of the proposed framework and potential future improvements are discussed.

2. Physics-Guided Transfer Learning for SFC Parameterization

2.1. Physical Formulation

The proposed transfer learning framework links the SWC and SFC formulations through a thermodynamic equivalence between drying-induced desaturation and freezing-induced liquid-water retention. Liquid-water potential ψ [Pa] serves as the common state variable of the SWC and SFC.

$$\psi = \psi_m + \psi_o \tag{1}$$

where ψ_m is the matric potential [Pa] and ψ_o is the osmotic potential [Pa]. ψ_m is negative under suction, and the matric suction head h [m] is related to ψ_m by

$$h = \frac{|\psi_m|}{\rho_l g} = -\frac{\psi_m}{\rho_l g} \tag{2}$$

where ρ_l is the density of liquid water [kg m^{-3}] and g is the gravitational acceleration [m s^{-2}].

2.1.1. Drying domain

For drying-induced desaturation, the osmotic effect is assumed negligible relative to matric suction, thus $\psi \approx \psi_m$. The SWCC is described using the van Genuchten relationship (van Genuchten 1980):

$$\theta_l = \theta_r^* + (\theta_s^* - \theta_r^*) \left[1 + (\alpha^* h)^{n^*}\right]^{-m^*} \tag{3}$$

$$m^* = 1 - 1/n^* \tag{4}$$

where θ_l is volumetric water content; θ_r^* is the residual water content; θ_s^* is the saturated water content; and α^* [m^{-1}], m^*, and n^* are fitting parameters. To distinguish the drying-domain and freezing-domain parameter sets, the VG parameters estimated from SWC curves are denoted as α^*, n^*, θ_r^*, and θ_s^*. The VG parameters calibrated for SFC curves are denoted without superscripts as α, n, θ_r, and θ_s.

2.1.2. Freezing domain

In frozen soils, the generalized Clausius-Clapeyron relation links temperature to liquid-water potential (Zhou et al. 2018). Neglecting external pressure gradient, equilibrium between ice and liquid water yields

$$\psi_{cryo} = \psi_o + \psi_m = \rho_l L_f \frac{T - T_0}{T_0} \tag{5}$$

where ψ_{cryo} is the cryogenic liquid-water potential [Pa], ρ_l is the liquid-water density [kg m^{-3}], L_f is the latent heat of fusion [J kg^{-1}], T is the soil temperature [K], and $T_0 = 273.15\ K$ is the freezing point of pure water at one atmosphere pressure. For $T < T_0$, ψ_{cryo} is negative.

The osmotic potential associated with dissolved solutes is expressed using water activity a_w (Chuvilin et al. 2022; Zhang et al. 2024):

$$\psi_o = \frac{RT}{V_m} \ln(a_w) \tag{6}$$

where R [J mol^{-1} K^{-1}] is the gas constant, and V_m [m^3 mol^{-1}] is the molar volume of water. $0 < a_w < 1$, and $\psi_o < 0$. The water activity is related to the osmotic coefficient ϕ_o through the Pitzer formulation (Pitzer 1975):

$$\ln(a_w) = -\nu m_c M_w \phi_o \tag{7}$$

where ν [-] is the number of ions per formula unit of dissolved salt ($\nu = 2$ for NaCl); $M_w = 0.018015$ kg mol^{-1} is the molar mass of water. The molality m_c is related to the molar liquid-water concentration c [mol m^{-3}] through

$$m_c = \frac{c}{M_{\text{salt}}\, \rho_l} \tag{8}$$

with M_{salt} [kg mol^{-1}] is the molar mass of the dissolved salt species. The osmotic coefficient ϕ_o is a function of ionic strength and temperature, evaluated from the ion-interaction formulation (Pitzer 1975) as adapted for frozen saline soils by Wu et al. (2023), with the Pitzer parameters and the Debye–Hückel coefficient A_ϕ expressed as polynomial functions of temperature (Spencer et al. 1990). Consequently, a_w becomes a function of temperature T and the pore-water salt concentration c.

Combining Eq. (2), Eq. (5) and Eq. (6), the equivalent matric suction head h_f [m] is:

$$h_f = -\frac{\psi_m}{\rho_l g} = -\frac{1}{\rho_l g}\left[\rho_l L_f \frac{T - T_0}{T_0} - \frac{RT}{V_m}\ln\left(a_w\right)\right] \tag{9}$$

Accordingly, the unfrozen water fraction θ_u can be expressed using the VG retention model by replacing the drying-domain matric suction head with h_f:

$$\theta_u = \theta_r + \left(\theta_s - \theta_r\right)\left[1 + \left(\alpha h_f\right)^n\right]^{-m} \tag{10}$$

The physics-guided layer uses four assumptions: laboratory specimens are homogeneous at the specimen scale; liquid-water movement and vapor transport are neglected during SFC curves fitting; water activity represents solute effects without explicitly resolving cryogenic concentration, salt precipitation, or concentration attenuation; liquid water and ice are assumed to remain in equilibrium at each temperature step.

2.2. Transfer Learning for SFC

The SFC transfer learning workflow consists of three components, including a pre-trained SWCC backbone, a residual adapter, and a physics-guided output layer (Figure 1). The workflow uses two groups of input variables. The first group is the shared soil-property vector $\mathbf{x}_s$, which contains soil properties used in both SWC pre-training and SFC adaptation. The second group is the freezing-domain property vector $\mathbf{x}_f$, which contains additional soil properties used only during SFC adaptation. The vector $\mathbf{x}_s$ contains eight variables, including sand content, silt content, clay content, dry density ρ_d, SOM, porosity φ, salinity M_s, and degree of saturation S_r. The vector $\mathbf{x}_f$ includes plastic limit (PL), liquid limit (LL), and specific surface area S_a.

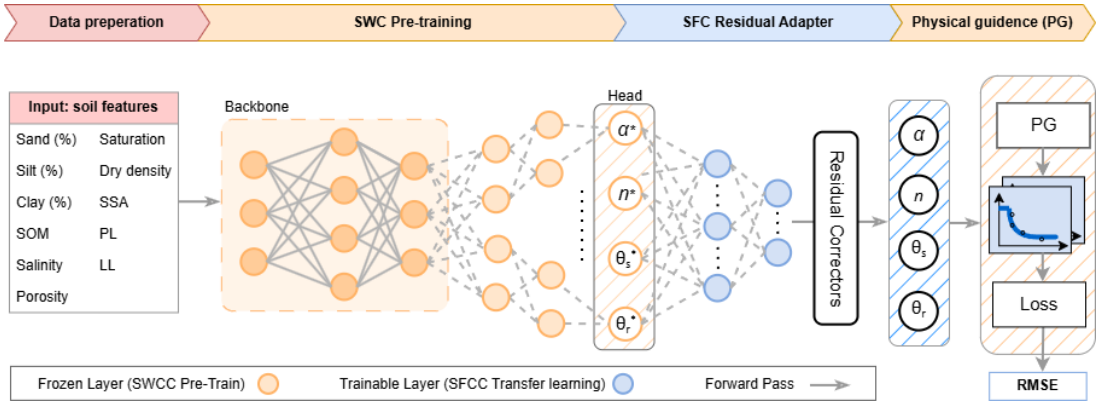


FIGURE 1. Architecture of the PG-TL framework, showing SWC pre-training, SFC residual adaptation, and the physics-guided GCE-VG output layer used to predict UWC.

The SWC backbone f_{θ^*} provides the baseline VG parameter estimate. It is initialized using weights obtained from SWC pre-training. The backbone takes the shared soil-property vector $\mathbf{x}_s$ as input and predicts the SWC-domain VG parameter vector $\mathbf{Y}^*_{VG} = [\alpha^*, n^*, \theta^*_r, \theta^*_s]$. The learned $\mathbf{Y}^*_{VG}$ is then passed through the physics-guided layer to reconstruct the SWC curves using Eq. (3). A fully connected neural network $f_{\theta*}$ predicts the $\mathbf{Y}^*_{VG}$ from these input features:

$$\mathbf{Y}^*_{VG} = f_{\theta*}\left(\mathbf{x}_s\right) \tag{11}$$

where $f_{\theta*}$ denotes the neural network after SWC pre-training. The architecture and training hyperparameters are summarized in Supplemental Materials **Text S3**.

The residual adapter g_θ adjusts the pretrained $\mathbf{Y}^*_{\mathrm{VG}}$ to the freezing-domain VG parameters $\mathbf{Y}_{VG} = [\alpha, n, \theta_r, \theta_s]$. The adapter uses both $\mathbf{x}_s$ and $\mathbf{x}_p$ as inputs. It predicts a correction vector $\Delta\mathbf{Y}_{VG}$,

$$\begin{aligned} \Delta\mathbf{Y}_{VG} &= [\Delta\log\alpha, \Delta\log n, \Delta\log\theta_r, \Delta\theta_s] \\ &= g_\theta([\mathbf{x}_s, \mathbf{x}_p]) \end{aligned} \tag{12}$$

Log-space corrections are used for α, n, and θ_r, and the saturated water content θ_s is corrected in linear space.

$$\mathbf{Y}_{VG} = \begin{bmatrix} \alpha^* \exp(\Delta\log\alpha) \\ n^* \exp(\Delta\log n) \\ \theta^*_r \exp(\Delta\log\theta_r) \\ \theta^*_s + \Delta\theta_s \end{bmatrix} \tag{13}$$

The physics-guided output layer converts $\mathbf{Y}_{\mathrm{VG}}$ and temperature T into the predicted UWC using the GCE–VG constitutive relation in Eq. (9) and Eq. (10). This layer contains no trainable parameters and serves as a physics-guided constitutive layer.

2.3. Model Calibration and Training Protocol

Both the SWC pre-training and SFC fine-tuning stages minimize the same loss function $\mathcal{L}$, which combines a standard mean squared error (MSE) term with a log-scale MSE term.

$$\mathcal{L} = \frac{1}{N}\sum_{k=1}^{N}\left(\widehat{\theta}_k - \theta_k\right)^2 + \frac{\lambda_{\log}}{N}\sum_{k=1}^{N}\left[\log\widehat{\theta}_k - \log\theta_k\right]^2 \tag{14}$$

where the variable $\widehat{\theta}_k$ is the predicted volumetric water content for the k-th training measurement, and θ_k is the corresponding measured value. In the SWC pre-training stage, $\widehat{\theta}_k$ represents the

predicted liquid water content θ_l. In the SFC fine-tuning stage, $\widehat{\theta}_k$ represents the predicted UWC θ_u. N is the number of training measurements. The coefficient $\lambda_{\log}$ controls the relative contribution of the log-scale error term. The two terms in loss function $\mathcal{L}$ emphasize different parts of water content range of SFC and SWC curves. The standard MSE term emphasizes errors where water content is high. The log-scale term gives more weight to low water contents, where small absolute errors can produce larger relative errors.

3. Governing Equations for Thermo-Hydro-Chemical Simulation

The PG-TL SFC parameterization was incorporated into a THC simulation of a 1D saline permafrost profile. The model was then used to evaluate coupled heat, liquid-water, and salt transport under climate boundary forcing.

- The hydraulic field is governed by pressure-based Richards equation. The PG-TL-derived GCE–VG parameterization uses soil index properties to partition the water and ice phases through the SFC curves and to compute hydraulic conductivity through the van Genuchten–Mualem function.
- The thermal field is governed by energy conservation with heat conduction and latent heat. Thermal conductivity is updated using phase contents and soil composition, including the insulating effect of organic matter and the influence of mineral texture.
- The chemical field is governed by mass conservation of dissolved salt in the liquid phase. The Pitzer model (Pitzer 1975) evaluates water activity and osmotic freezing-point depression in saline pore water, linking the salt concentration to matrix suction and water–ice partitioning.

3.1. THC Formulation

3.1.1. Energy conservation

Energy conservation incorporates conductive heat transfer, latent heat effects during phase change, and sensible heat advection by liquid flow,

$$(\rho C)_{\text{app}} \frac{\partial T}{\partial t} + \rho_l c_l \mathbf{u}_D \frac{\partial T}{\partial z} = \frac{\partial}{\partial z}\left(\lambda_{\text{eff}} \frac{\partial T}{\partial z}\right) \tag{15}$$

The λ_{eff} is determined by a Johansen-type normalized thermal conductivity model (Johansen 1977), Farouki soil thermal conductivity formulation (Farouki 1981), with organic extension (Lawrence and Slater 2008); the specific implementation follows Lawrence et al. (2020). The $(\rho C)_{app}$ is the apparent volumetric heat capacity [J m^{-3} K^{-1}], c_l is the specific heat capacity of

liquid water [J kg^{-1} K^{-1}], $\mathbf{u}_D$ is Darcy's velocity [m s^{-1}] obtained from the Richards equation, λ_{eff} is the effective thermal conductivity [W m^{-1} K^{-1}].

Latent-heat release and uptake during phase change are incorporated into the apparent heat capacity as

$$(\rho C)_{app} = (\rho C)_{sens} + \rho_l L_f \left| \frac{\partial \theta_u}{\partial T} \right| \tag{16}$$

where the sensible volumetric heat capacity $(\rho C)_{sens} = \sum_x \theta_x \rho_x c_x$ [J m^{-3} K^{-1}], and $x = m,\ o,\ l, i$ (mineral, organic, liquid-water, and ice phase); ρ_l is the density of liquid water [kg m^{-3}]; L_f is the specific latent heat of fusion of water [J kg^{-1}].

3.1.2. Water migration

Neglecting evaporation and assuming an immobile ice phase, conservation of total water mass is

$$\frac{\partial \Theta}{\partial t} = -\frac{\partial \mathbf{u}_D}{\partial z} \tag{17}$$

$$\Theta = \theta_u + \frac{\rho_i}{\rho_l}\theta_i \tag{18}$$

where Θ is the liquid-water-equivalent total water content, ρ_l and ρ_i are the densities of liquid water and ice that are assumed as constants, and z [m] is the vertical coordinate taken positive downward. The quantity in parentheses represents the conserved liquid-water-equivalent total water content,

p is identified with the matric-potential pressure (i.e., $p = \psi_m$). The Darcy velocity $\mathbf{u}_D$ is written as

$$\mathbf{u}_D = -\frac{K_{eff}}{\rho_l g}\left(\frac{\partial p}{\partial z} - \rho_l g\right) \tag{19}$$

where K_{eff} [m s^{-1}] is the effective hydraulic conductivity, defined as

$$K_{eff} = K_s K_r I_{imp} \tag{20}$$

K_s [m s^{-1}] is the saturated hydraulic conductivity, parameterized following the Community Land Model (CLM) soil hydrology scheme (Lawrence et al. 2020) to account for mineral–organic mixing; $I_{\text{imp}} = 10^{-10\theta_i}$ [-] is the ice-impedance factor that progressively suppresses

liquid mobility as pore ice develops (Hansson et al. 2004); and K_r [-] is the relative hydraulic conductivity following the van Genuchten–Mualem formulation (Mualem 1976).

$$K_r = S_e^{\ell}\left[1-\left(1-S_e^{1/m}\right)^{m}\right]^2, \quad S_e = \frac{\theta_u-\theta_r}{\theta_s-\theta_r} \tag{21}$$

where S_e [-] is the effective liquid saturation; ℓ [-] is the Mualem pore-connectivity parameter.

3.1.3. Dissolved salt migration

Dissolved salt transport in the liquid phase is formulated using the bulk-volume dissolved salt molar concentration M_s [mol m^{-3}], which is related to the liquid-phase molar concentration c [mol m^{-3}] by $M_s = \theta_u\, c$.

The governing equation is

$$\frac{\partial M_s}{\partial t} + \frac{\partial J_s}{\partial z} = 0, \qquad J_s = \mathbf{u}_D c - D_{\text{eff}}\frac{\partial c}{\partial z} \tag{22}$$

where J_s [mol m^{-2} s^{-1}] is the total salt molar flux, comprising advective and diffusive components; and D_{eff} [m^2 s^{-1}] is the bulk effective diffusion coefficient for dissolved NaCl in the partially saturated pore space. The diffusion coefficient is corrected for partial saturation through the Millington–Quirk tortuosity relation (Millington and Quirk 1961),

$$D_{eff} = D_{salt}\frac{\theta_u^{7/3}}{\varphi^2}, \tag{23}$$

where D_{salt} [m^2 s^{-1}] is the molecular diffusion coefficient of dissolved salt in free water.

3.2. Boundary Conditions

The PG-TL SFC parameterization was incorporated into the THC simulation for a saline permafrost column. The soil column is assumed one-dimensional with depth of 10 m ($0 \le z \le L,\ L = 10\ m$). The upper thermal and hydraulic boundaries ($z = 0$) were computed by the CryoGrid community model using a surface energy balance coupled with bucket-scheme snow hydrology (Westermann et al. 2016, 2023). Incoming shortwave and longwave radiation were balanced against turbulent sensible and latent heat fluxes at the snow or ground surface, with turbulent exchange evaluated using Monin-Obukhov similarity theory and empirical stability corrections (Dyer 1974; Monin and Obukhov 1954). The model was driven by standard atmospheric forcing, including incoming shortwave and longwave radiation, air temperature, wind speed, humidity, rainfall, snowfall, and air pressure. Snow-covered and snow-free surface states evolved through snow accumulation, meltwater routing, and snow thermal resistance,

which regulated the heat and water fluxes into the soil column. The heat and liquid-water boundary fluxes computed by the CryoGrid boundary module are denoted as $F_{CG}(t)$ and $q_{CG}(t)$, respectively. At the top boundary, $F_{CG}(t)$ ($W\,m^{-2}$) was imposed as a Neumann heat-flux boundary and $q_{CG}(t)$ ($m\,s^{-1}$) was imposed as the upper hydraulic flux:

$$-\lambda_{eff}\left.\frac{\partial T}{\partial z}\right|_{z=0} = F_{CG}(t) \tag{24}$$

$$\mathbf{u}_D(z,t)\big|_{z=0} = q_{CG}(t) \tag{25}$$

At $z = 10\ m$, a fixed-temperature Dirichlet boundary condition was imposed to the lower thermal boundary, and the lower hydraulic boundary was set to no flow:

$$T(z,t)\big|_{z=L} = T_b(t) \tag{26}$$

$$\mathbf{u}_D(z,t)\big|_{z=L} = 0 \tag{27}$$

where $T_b(t)$ was approximated using the observed ground-temperature record at approximately 10 m depth from a borehole located near the field site for the THC simulation (Romanovsky et al. 2019).

For the salt intrusion scenario, solute exchange at the upper boundary was represented using a third-type Cauchy boundary condition, following the HYDRUS formulation (van Genuchten and Parker 1984). Marine salt loading was represented by a surface reservoir with a constant seawater-strength concentration of $c_{sw} = 600\ mol\ m^{-3}$. The water flux prescribed by the surface-bucket hydraulic boundary determined the direction of advective solute transport.

3.3. Numerical Implementation

At the beginning of each time step t^n, the model state is defined by temperature T^n, pressure p^n, bulk salinity M_s^n, liquid-phase salinity c^n, and the VG parameter vector. These variables are advanced to t^{n+1} through a sequential hydraulic, chemical, thermal, and constitutive update procedure (Figure 2).

The hydraulic field is solved first using equation in Eq. (17)-Eq. (19). During this step, T^n, c^n, and VG^n are held fixed, and a mass-conservation Picard iteration is applied to update p. At Picard iteration k, the GCE-VG relation is evaluated with the current pressure iterate to obtain

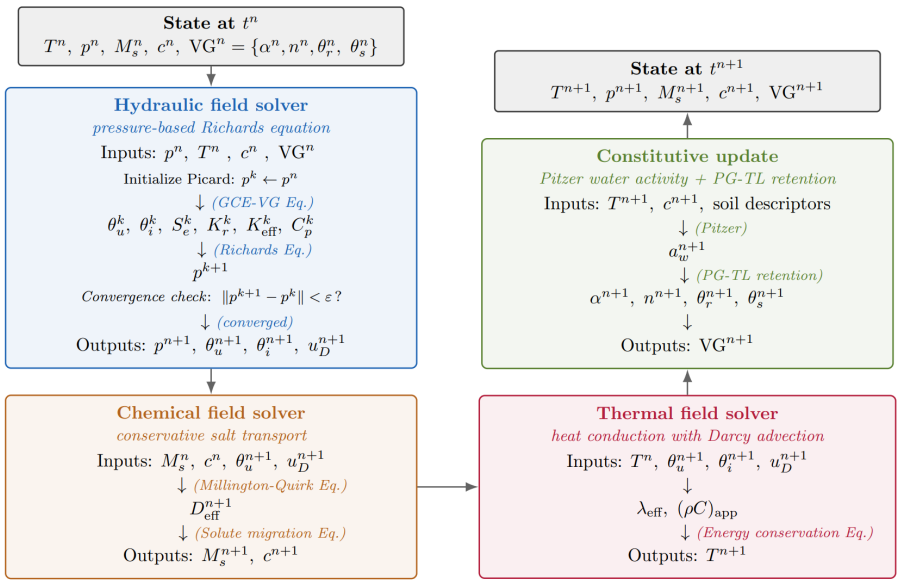


FIGURE 2. Algorithm for advancing the coupled THC simulator from t^n to t^{n+1}, including hydraulic, chemical, thermal, and constitutive-update steps.

the θ_u^k, S_e^k, I_{imp}^k, and K_{eff}^k. Because T, c, and the VG parameters are fixed within this hydraulic substep, the liquid-water storage term is linearized with respect to pressure as

$$\frac{\partial \theta_u}{\partial t} \approx \left(\frac{\partial \theta_u}{\partial p}\right)^k \frac{p^{k+1} - p^n}{\Delta t} \tag{28}$$

The updated pressure field gives the Darcy flux $\mathbf{u}_D^{k+1}$, which is then used to advance the conserved liquid-water-equivalent total water content,

$$\Theta^{k+1} = \Theta^n - \Delta t \frac{\partial \mathbf{u}_D^{k+1}}{\partial z}, \Theta = \theta_u + \frac{\rho_i}{\rho_l}\theta_i \tag{29}$$

The ice content is updated from the residual phase balance,

$$\theta_i^{k+1} = \frac{\rho_l}{\rho_i}\left(\Theta^{k+1} - \theta_u^{k+1}\right) \tag{30}$$

After Picard convergence, the hydraulic solver returns p^{n+1}, θ_u^{n+1}, θ_i^{n+1}, Θ^{n+1}, and $\mathbf{u}_D^{n+1}$. The corresponding phase-change rate used in the thermal update is evaluated by backward difference as

$$\left(\frac{\partial \theta_i}{\partial t}\right)^{n+1} \approx \frac{\theta_i^{n+1} - \theta_i^n}{\Delta t} \tag{31}$$

The chemical field is then updated using M_s^n, c^n, θ_u^{n+1}, and $\mathbf{u}_D^{n+1}$. Dissolved salt is governed by the solute conservation equation in Eq. (22). The effective diffusion coefficient D_{eff}^{n+1} is calculated using the Millington-Quirk relation in Eq. (23). This step updates the conserved bulk salt concentration M_s^{n+1} and the liquid-phase concentration c^{n+1}.

The thermal field is solved after the hydraulic and chemical updates. The energy conservation equation in Eq. (15) uses T^n, θ_u^{n+1}, θ_i^{n+1}, and $\mathbf{u}_D^{n+1}$ as inputs. The effective thermal conductivity λ_{eff} and the apparent volumetric heat capacity $(\rho C)_{app}$ are evaluated from the current phase contents and soil properties. The thermal update accounts for heat conduction, latent heat associated with water–ice phase change, and sensible-heat transport by the Darcy flux. This step gives the updated temperature T^{n+1}.

A constitutive update is then performed before the next time step. The Pitzer model uses T^{n+1}, c^{n+1}, and θ_u^{n+1} to calculate water activity a_w^{n+1}. The PG-TL model then updates the VG parameters α^{n+1}, n^{n+1}, θ_r^{n+1}, and θ_s^{n+1}. The updated parameter vector VG^{n+1} is used in the GCE–VG relation at the next time step. The final state at $t^{n+1}$is therefore $\left[T^{n+1}, p^{n+1}, M_s^{n+1}, c^{n+1}, VG^{n+1}\right]$.

4. Data Sources and Model Inputs

4.1. SFC Dataset Compilation

The SFC dataset was compiled from 45 publications (listed in Supplemental Materials **Text S1**). For each sample, thirteen soil index properties were compiled and classified into four groups based on their physical characteristics. The texture group includes sand, silt, and clay contents based on the USDA grain-size limits. Sand is defined as particles larger than $0.05\,mm$, silt as 0.002–$0.05\,mm$, and clay as particles smaller than $0.002\,mm$. The phase-relation group includes dry density ρ_d, porosity φ, degree of saturation S_r, specific gravity G_s, and total volumetric water content θ_{tot}. The surface and plasticity group includes specific surface area S_a, plastic limit PL, and liquid limit LL. The chemical and organic group includes soil organic matter SOM and pore-water salinity M_s. Published investigations of SFC observations may only report a subset of the soil metadata needed for model development. To retain as many compiled samples as possible, missing metadata were completed in two steps, as described in Supplemental Materials **Text S2**. Eleven of these properties are direct inputs to the PG-TL model, namely, the sand, silt, and clay fractions, ρ_d, φ, S_r, S_a, SOM, M_s, PL, and LL. The

remaining two (G_s and θ_{tot}) are not used as model inputs but are retained for the subsequent missing-metadata recovery.

After metadata recovery and imputation, the final SFC dataset included 290 soil samples and 4,528 temperature–UWC observations. Only freezing measurements were included and supercooling-affected data points were removed. Among the 290 samples, 48 are classified as organic (SOM $\geq$ 1%) and 63 as saline ($M_s \geq 0.01$ mol L^{-1}). The distribution across USDA textural classes and key input variables are summarized in Figure 3.

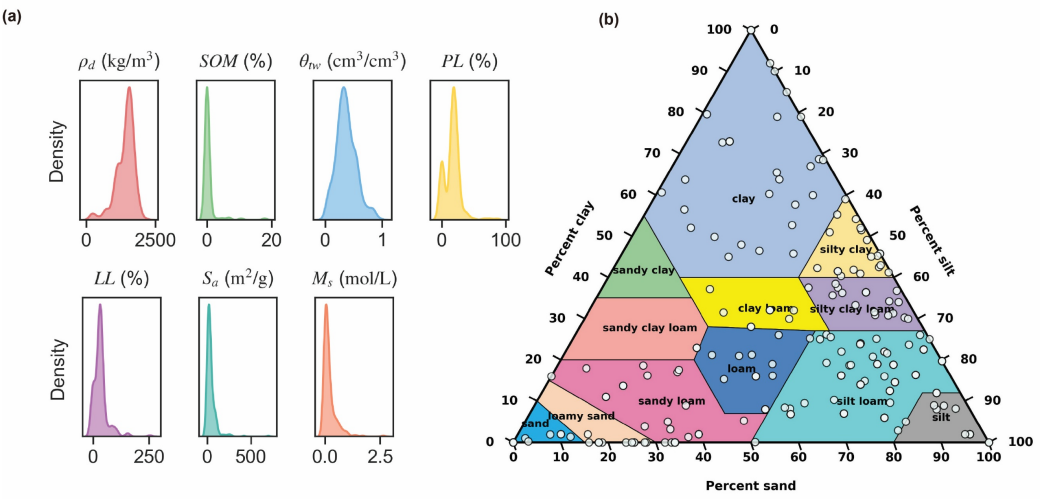


FIGURE 3. SFC database summary: (a) probability density functions of selected input variables; and (b) USDA textural classes.

Hyperparameters were tuned using Bayesian optimization implemented in Optuna (Akiba et al. 2019). The Tree-structured Parzen Estimator (TPE) sampler was used to select candidate configurations. Each trial was evaluated using five-fold cross-validation grouped by soil sample (Fushiki 2011). The search space and the optimized values are reported in Supplemental Materials **Text S3.**

4.2. SWC Dataset for Pre-training

The SWC measurements used for pre-training were extracted from the UNSODA 2.0 database (Nemes et al. 2001), a publicly available compilation of unsaturated soil hydraulic data from 790 soil samples collected worldwide. The water retention measurements in UNSODA were obtained using standard laboratory methods, including Tempe cells, hanging water columns, pressure plates, and pressure outflow devices. The soil properties retained for pre-training, all of which are reported in or directly derivable from UNSODA, included sand content, silt content, clay content, SOM (%), ρ_d (kg/m^3), electrical conductivity of the soil solution (S/m), G_s(-),

and φ (-). To maintain consistency with the laboratory-based SFC dataset, only laboratory drying records were retained, and observations with $h > -10$ cm were excluded to avoid the near-saturation range where measurement uncertainty is large and capillary effects are not yet fully developed. After filtering, the pre-training dataset comprised 718 soil samples and 7943 pressure head–water content observations. Among the retained samples, SOM ranged from 0 to 88.4%, with 52.3% of samples reporting non-zero values. Eight samples with SOM between 21.4% and 88.4% correspond to peat or highly organic soils. Excluding the eight highly organic samples, SOM of remaining samples ranges from 0 to 14.48%, with a mean of 0.82% and a median of 0.08%.

4.3. Climate Forcing and Ground Conditions for THC Simulation

The simulations were configured for a field site near Utqiaġvik, Alaska, where low-relief coastal tundra is underlain by continuous permafrost (Lara et al. 2018). The surrounding landscape is characterized by wet to moist graminoid–moss vegetation, drained lake basin and coastal plain terrain, and organic surface layer over silty clay loam, loam, and gravelly loam mineral soils (Bockheim et al. 2001; Hinkel and Nelson 2003). The site contains spatially heterogeneous pore-water salinity, ranging from fresh to elevated salinity that generally increases with depth (Brown 1969). Borehole temperature observations at depths of 0.15 m and 1.5 m at a monitoring site located at 71.329°N, 156.593°W (Nicolsky and Wright 2024 2025) were used to constrain the surface energy-balance parameterization and evaluate model performance over August 2022 to July 2025. Electrical resistivity tomography (ERT) imaging at a nearby site (Tourei et al. 2024) provided an additional constraint on subsurface stratigraphic delineation. The 1D stratigraphy used in the coupled THC simulation was parameterized by combining three complementary data sources: measured soil index and thermal properties from borehole S4 (Wang et al. 2026), co-located ERT-derived stratigraphic interpretations (Tourei et al. 2024), and vertical profiles of organic content from nearby boreholes (Farley et al. 2026). Layer-averaged soil properties used in the model are summarized in Table 1.

Hourly meteorological forcing was obtained from the ERA5 atmospheric reanalysis (Hersbach et al. 2020) at the nearest 0.25° grid point to the study site (71.3°N, 156.8°W), including air temperature at 2 m above ground, wind speed at 10 m above ground, surface pressure, dew-point temperature at 2 m above ground (converted to specific humidity), downward shortwave and longwave radiation, total precipitation, snowfall, and snow depth. All variables were retrieved at hourly resolution for the period of August 2022 through December 2025 and used as inputs to the surface energy-balance scheme that provided the upper boundary forcing for the THC simulator.

TABLE 1. Layered soil properties used to parameterize the 1D borehole simulation and PG-TL SFC parameterization.

Layer*	Depth (m)	Sand (%)	Silt (%)	Clay (%)	SOM (g g^{-1})	Dry density (kg m^{-3})	Salinity (mol L^{-1})	Porosity (-)	Saturation (-)	PL (%)	LL (%)	S_a (m^2 g^{-1})
1	0.25	36	62	2	0.200	334	0.004	0.87	0.97	14.5	20.8	51.3
2	0.50	67	33	0	0.031	430	0.014	0.80	0.98	23.0	26.0	7.9
3	1.40	76	24	0	0.009	570	0.035	0.78	0.94	23.7	26.0	6.3
4	4.00	76	24	0	0	1380	0.300	0.48	0.95	NP	NP	5.5
5	10.0	76	24	0	0	1380	0.000	0.48	0.95	NP	NP	5.5

* Layers 1~5 represent the organic-rich active layer, ice rich silt, ice-rich sand, high-salinity sand, and ice-poor sand. **NP denotes non-plastic Atterberg limits.

5. Results and Discussion

5.1. Validation of the PG-TL model

The PG-TL model was tested under sample-grouped five-fold cross-validation, with an out-of-fold R^2 of 0.873 and an RMSE of $0.054\,m^3\,m^{-3}$. The SFC prediction was evaluated against published measurements in which key soil properties were varied independently, including M_s, SOM, ρ_s, and S_r (Figure 4). The comparisons were used to evaluate the physical consistency of PG-TL model in providing SFC parameterizations for the subsequent THC simulations. The predictions generally followed the measured responses for the four soil properties. Increasing salinity depresses the freezing point and increases UWC at a given subzero temperature (Figure 4a). Higher soil organic matter and larger specific surface area increase unfrozen water retention, particularly at moderate to low subzero temperatures (Figure 4b and c). Higher initial saturation mainly increases UWC near the freezing point, with a weaker effect at lower temperatures (Figure 4d).

5.2. Application of Thermo-Hydro-Chemical Simulation

Four THC simulation scenarios are designed to evaluate different disturbance conditions and are summarized in Table 2. Scenario 0 (baseline) represents undisturbed conditions and is used for model calibration. Scenario 1 imposes sustained surface salinization from the top of organic horizon while keeping the soil profile unchanged. Scenario 2 combines surface salinization with organic-layer removal after the first simulation year by setting the SOM of Layers 1 and 2 (listed in Table 1) to zero. Scenario 3 imposes organic-layer removal without surface salinization and is designed to isolate the effect of organic-layer removal from the combined disturbance in Scenario 2.

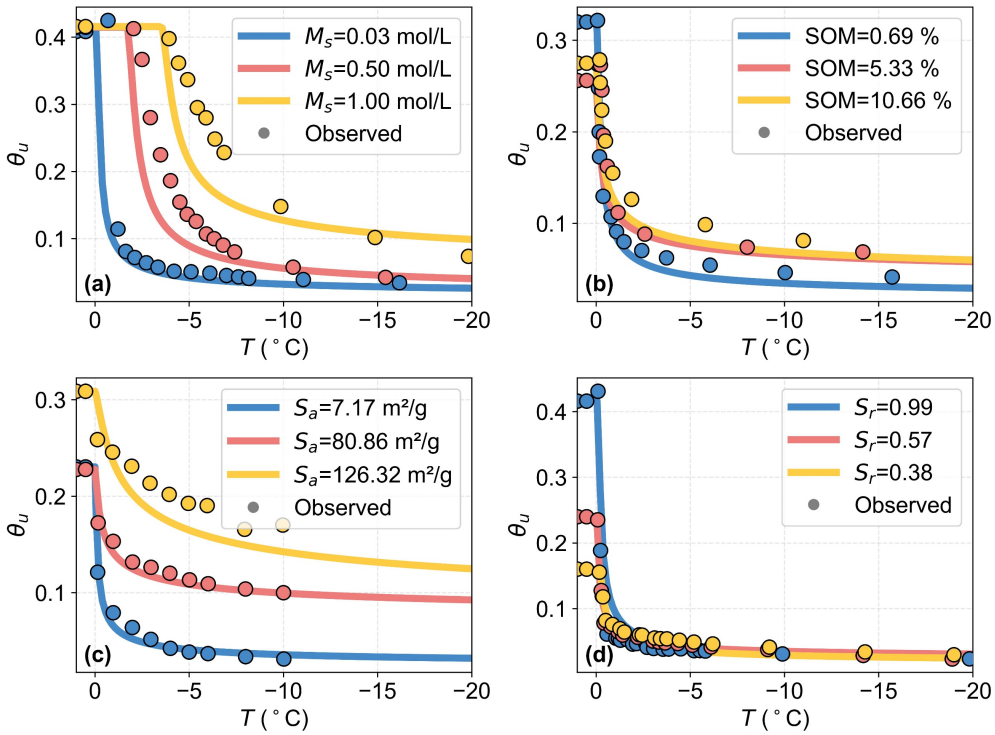


FIGURE 4. Model predictions versus published measurements for four soil properties. (a) salinity M_s (Meng et al. 2020), (b) soil organic matter (SOM) (Chuvilin et al. 2022), (c) specific surface area S_a (Christ et al. 2009), and (d) initial saturation S_r (Zhou et al. 2020).

TABLE 2. Design of four simulation scenarios and resulting annual maximum thaw depths (m). Each scenario combines two disturbance pathways under different on/off conditions, isolating the individual and combined effects of surface salinization and organic-layer removal on saline permafrost thermal response.

Scenario	Salini-zation	Organic-layer removal	Annual thaw depths (m)				Purpose
			2022	2023	2024	2025	
S0	—	—	0.341	0.491	0.384	0.365	Baseline (undisturbed)
S1	Years 1–3	—	0.341	0.494	0.415	0.390	Salinization only
S2	Years 1–3	Years 2–3	0.341	0.491	0.488	0.490	Combined disturbance
S3	—	Years 2–3	0.341	0.490	0.446	0.465	SOM removal only

For each model layer, the PG-TL model used the layer-averaged soil index properties summarized in Table 1 to estimate the VG parameters and generate the corresponding site-specific SFC parameterization. Laboratory SFC measurements are available only for permafrost core samples collected from approximately 0.2 to 1.7 m depth near Utqiaġvik, Alaska (Wang et al. 2026). These SFC measurements are used to assess the SFC curves prediction. The comparison in Figure 5 shows that the PG-TL predictions are generally consistent with the laboratory measurements. Shallow permafrost at 60–80 cm depth exhibits slightly higher θ_r, consistent with their relatively higher organic matter content. Permafrost at 150 cm depth has lower ice content and reduced porosity, while pore-water salinity reaches approximately 0.14 mol/L. The elevated solute concentration depresses the freezing point and increases the residual unfrozen water, which is reflected in the fitted PG-TL parameters by decreased a_w, α, and n, and increased θ_r (Figure 5).

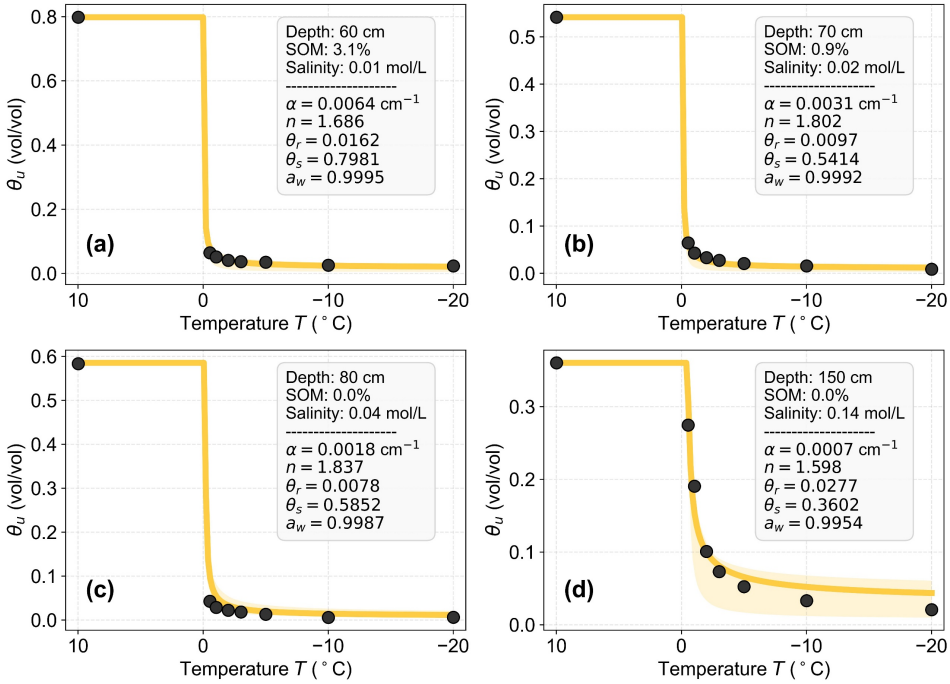


FIGURE 5. Comparison of predicted and measured SFCs of permafrost samples in Utqiaġvik, Alaska at depths of (a) 60 cm, (b) 70 cm, (c) 80 cm, and (d) 150 cm.

Model performance under the undisturbed baseline scenario was first evaluated against borehole temperature observations at 0.15 and 1.5 m depths (Nicolsky and Wright 2024, 2025) (Figure 6). Annual active layer thickness (ALT) observations from two nearby CALM sites in Utqiaġvik

(U1 and U2, both at 71.317°N, 156.6°W) were averaged to provide a validation against the simulated annual maximum thaw front (CALM 2024). The thaw front was defined based on liquid-water fraction; and a layer was considered thawed when $\theta_u/\theta_{tot} > 0.95$. The thaw front was taken as the deepest layer meeting this criterion. Figure 7 shows the evolution of thermal, hydraulic, and chemical fields in Scenario 0, which serves as a reference case for evaluating the perturbation responses in Scenarios 1 to 3. Only the top 2-m profiles are shown due to the lack of variations beneath 2 m.

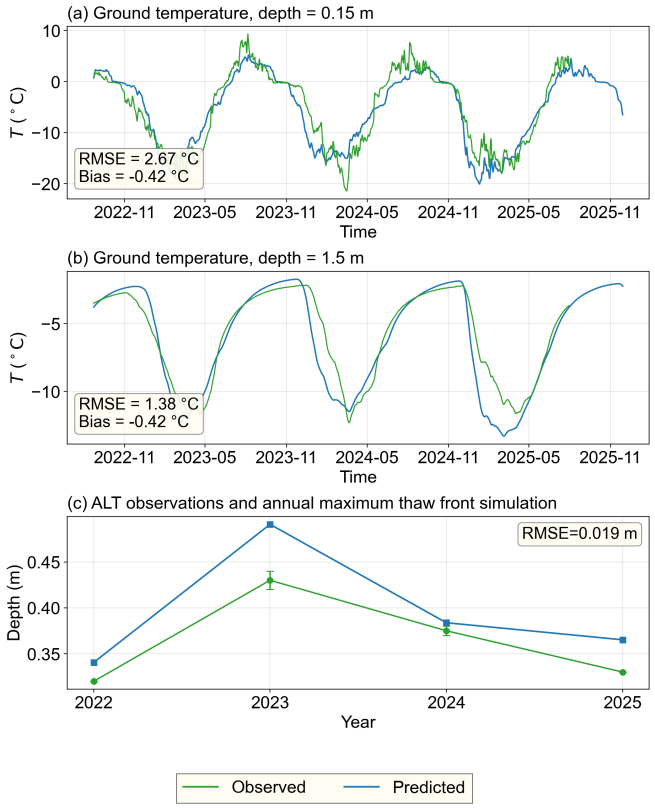


FIGURE 6. Validation of simulated permafrost thermal regime in Utqiaġvik, Alaska at (a) 0.15 m and (b) 1.5 m depths, with observations from Nicolsky and Wright (2024, 2025). (c) Simulated annual maximum thaw front compared with regional active-layer-thickness measurements from CALM network (CALM 2024).

The perturbation scenarios are compared in Figure 8. The upper panels show the time-depth evolution of NaCl-equivalent dissolved salt volume fraction $\theta_{salt,\ diss}$ under salt intrusion (Scenario 1) and under combined salt intrusion and organic-layer removal (Scenario 2). The vertical dashed line in Scenario 2 in Figure 8 (a) marks the onset of organic-layer removal at

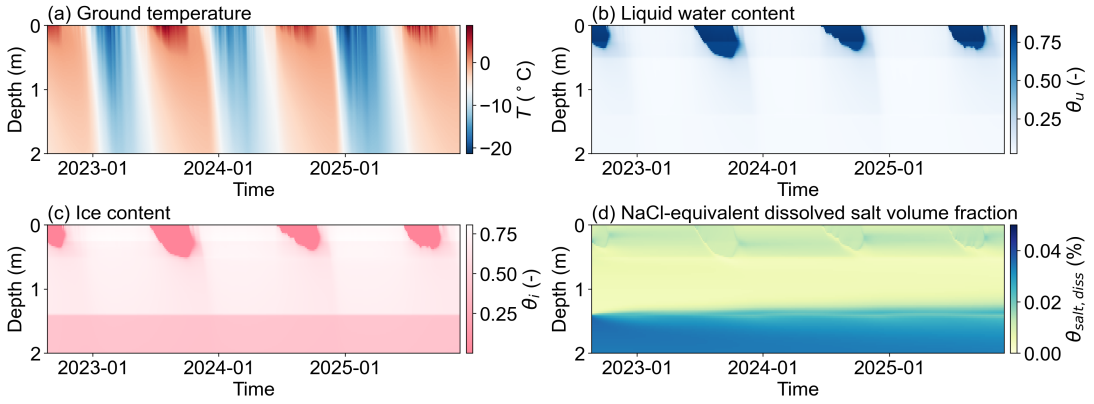


FIGURE 7. Three-year simulated time–depth evolution of (a) ground temperature, (b) liquid water content, (c) ice content, and (d) NaCl-equivalent dissolved salt volume fraction $\theta_{salt,\ diss}$ from the 1D borehole model in Utqiaġvik, Alaska for Scenario 0.

the beginning of the second simulation year. Figure 8 (c) and (d) summarize the resulting thaw-front evolution and the ground temperature response at 1 m depth for all four scenarios, including the undisturbed baseline.

The four simulated scenarios produced distinct active layer responses (**Figure 8, Table 2**). In 2022, all cases had the same maximum thaw depth of 0.3405 m because the imposed disturbances had not yet substantially affected the thawing front. Salt infiltration was also limited during the first winter, as ice formation reduced liquid saturation and suppressed hydraulic conductivity. Differences of thaw depth became more pronounced in 2024 and persisted into 2025. Salt intrusion (Scenario 1) produced a moderate increase in the maximum thaw depth, from 0.3837 to 0.4148 m in 2024 and from 0.3651 to 0.3898 m in 2025, corresponding to increases of 8.1% and 6.8% relative to the baseline scenario. Organic-layer removal produced a larger simulated response (Scenario 3), with thaw depths of 0.4461 m in 2024 and 0.4649 m in 2025, 16.3% and 27.3% above the baseline, respectively. The combined disturbance (Scenario 2) resulted in the deepest simulated thaw front, reaching 0.4883 m in 2024 and 0.4904 m in 2025, equivalent to increases of 27.3% and 34.3%, respectively. These THC simulation results suggest that organic-layer removal mainly affects the depth of seasonal heat penetration, whereas salinization affects the persistence of liquid water under subzero conditions. The combined response appears approximately additive over the simulated period.

The simulated 1D distributions of T, θ_u, and $\theta_{salt,dis}$ in Figure 8 (c), (d) illustrate the interactions of thermal, hydraulic, and solute fields within the active layer. Two dates were selected, 2024-12-31 near the deep-winter minimum thaw depth and 2025-09-13 at the maximum thaw depth.

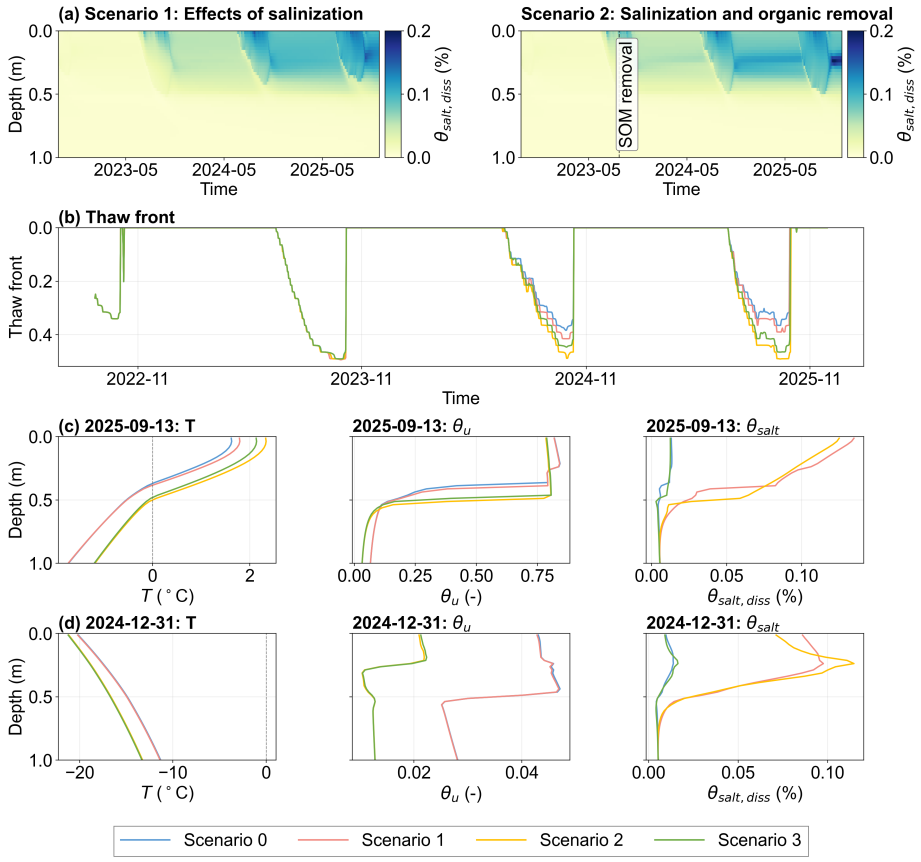


FIGURE 8. Simulated salinity redistribution, thaw-front evolution, and seasonal profile responses of the 1D borehole model at Utqiaġvik, Alaska, under disturbance scenarios. (a) Time-depth evolution of NaCl-equivalent dissolved salt volume fraction under Scenario 1 (salt intrusion only; left) and Scenario 2 (salt intrusion followed by SOM removal; right). (b) Thaw-front evolution for Scenarios 0–3. (c) Profiles of temperature, UWC, and dissolved salt volume fraction on the 2025 maximum-thaw day. (d) Corresponding profiles on a representative 2024 winter day.

Organic-layer removal dominated the thermal response in both seasons. Scenarios 2 and 3 were warmer in summer and colder in winter than the organic-retained scenarios throughout the upper 1 m, by approximately 1.5 °C at 0.25 m in December. The organic layer therefore acts as a bidirectional insulator against both summer heat and winter cold. During the freezing period, UWC decreased in response to the colder thermal state caused by organic-layer removal, with θ_u reduced by approximately 1–3% relative to the organic-retained scenarios. During the thawing period, dissolved salt increased with depth in the upper 0.5 m, consistent with downward infiltration from the surface reservoir. In winter, the elevated salt concentrated in near 0.25 m. This pattern is consistent with salt exclusion at advancing freezing fronts and the upward migration of solutes with capillary water during freeze-up (Brouchkov 2003; Wan et al. 2019).

5.3. Limitations and further improvements

Several limitations of the present study should be noted and considered for future work. First, available SFC measurements remain limited for complex geotechnical environments where salinity, soil texture, and organic matter must be considered together. This limitation is particularly important for organic-rich and saline frozen soils, where direct measurements are still sparse. The compiled data are also largely based on laboratory-characterized soils. They may therefore underrepresent intact field fabric, cryostructure, and in situ pore-scale heterogeneity. Future work should expand the SFC database with samples collected from instrumented boreholes, cryostructure-characterized samples, and targeted SFC measurements on underrepresented frozen soil types. In addition, hydraulic conductivity was estimated using the Mualem–van Genuchten relation; validation of this relation for frozen saline soils against direct hydraulic conductivity measurements is beyond the scope of this study. For samples with reported pore-water solution, sodium and chloride were the dominant ions. Therefore, salinity was represented using NaCl concentration in the present framework. The model does not explicitly resolve multi-ion chemistry or ion-specific interactions with mineral and organic surfaces, which may be important in other chemically complex Arctic and coastal soils.

The 1D THC application does not resolve lateral advective transport, snow-vegetation-atmosphere feedback, mechanical deformation, and thaw settlement. Extending the simulator to two- and three-dimensional domains, coupling it with land-surface and mechanical modules, and representing organic-layer loss as a progressive degradation process would enable more realistic representation of permafrost evolution under combined disturbances.

6. Conclusions

This study developed a coupled THC simulation workflow for saline, organic-rich permafrost, supported by a PG-TL-based SFC parameterization derived from soil index properties. The transfer learning strategy used a PTF pre-trained on 718 SWCC samples to constrain VG-parameter estimation and then adapted the learned representation to 290 SFCC samples. Sample-grouped five-fold cross-validation yielded an out-of-fold $R^2$of 0.873 and an RMSE of 0.054. Controlled comparisons further showed that the PG-TL model reproduced the main effects of salinity, soil organic matter, specific surface area, and initial saturation on SFC behavior.

The THC simulations indicate that salt intrusion and organic-layer removal jointly impact the near-surface hydrothermal state of saline permafrost. Salt intrusion increased unfrozen water persistence at subzero temperatures, whereas organic-layer removal reduced near-surface insulation and allowed seasonal heat to penetrate deeper into the subsoil. In the salt-intrusion scenario, the salinity perturbation remained mainly within the active layer. Its influence on active layer deepening became more evident in the second simulation year, indicating a delayed thaw response as seasonal thawing restored liquid-water pathways for salt transport. Over the three-year simulation period, the effects of salt intrusion and organic-layer removal appeared approximately additive. By the third summer, the annual maximum active-layer thickness reached 106.8%, 127.3%, and 134.3% of the undisturbed baseline in the salt-intrusion, organic-removal, and combined-disturbance scenarios, respectively.

Data Availability

The trained PG-TL model is publicly available on GitHub (`https://github.com/xuey61/pg-tl-sfcc.git`). The SWC and SFC databases and site-specific THC simulation data are available from the corresponding author upon request.

Acknowledgments

X. Wang and M. Xiao were supported by the National Science Foundation under Awards CMMI-2034363, RISE-1927718, RISE-2527154.

Author Contributions

Xueyang Wang: Conceptualization; Data curation; Formal analysis; Investigation; Methodology; Resources; Software; Validation; Visualization; Writing– original draft; Writing– review and editing. Ming Xiao: Conceptualization; Funding acquisition; Investigation; Resources; Supervision; Writing– review and editing.

Supplemental Materials

Text S1–S3 are provided in the Supplemental Materials (`https://github.com/xuey61/pg-tl-sfcc/tree/main/docs`).

References

Akiba, T., S. Sano, T. Yanase, T. Ohta, and M. Koyama. 2019. "Optuna: a next-generation hyperparameter optimization framework." In: *Proceedings of the 25th ACM SIGKDD International Conference on Knowledge Discovery & Data Mining*, KDD '19, 2623–2631. New York, NY, USA: Association for Computing Machinery.

Amankwah, S. K., A. M. Ireson, C. Maulé, R. Brannen, and S. A. Mathias. 2021. "A model for the soil freezing characteristic curve that represents the dominant role of salt exclusion." *Water Resources Research*, 57 (8): e2021WR030070. https://doi.org/10.1029/2021WR030070.

Anderson, D. M., and A. R. Tice. 1973. "The unfrozen interfacial phase in frozen soil water systems." *Physical Aspects of Soil Water and Salts in Ecosystems*, edited by A. Hadas, D. Swartzendruber, P. E. Rijtema, M. Fuchs, and B. Yaron, 107–124. Berlin, Heidelberg: Springer.

Benson, C. H., I. Chiang, T. Chalermyanont, and A. Sawangsuriya. 2014. "Estimating van Genuchten parameters α and n for clean sands from particle size distribution data." 410–427. American Society of Civil Engineers. https://doi.org/10.1061/9780784413265.033.

Bi, J., G. Wang, Z. Wu, H. Wen, Y. Zhang, G. Lin, and T. Sun. 2023. "Investigation on Unfrozen Water Content Models of Freezing Soils." *Frontiers in Earth Science*, 10. https://doi.org/10.3389/feart.2022.1039330.

Black, P. B., and A. R. Tice. 1989. "Comparison of Soil Freezing Curve and Soil Water Curve Data for Windsor Sandy Loam." *Water Resources Research*, 25 (10): 2205–2210. https://doi.org/10.1029/WR025i010p02205.

Bockheim, J. G., K. M. Hinkel, and F. E. Nelson. 2001. "Soils of the Barrow region, Alaska [1]." *Polar Geography*, 25 (3): 163–181. https://doi.org/10.1080/10889370109377711.

Brouchkov, A. 2003. "Frozen saline soils of the Arctic coast: their distribution and engineering properties." In: *In Proceedings of the eighth international conference on permafrost, Zurich, Switzerland (Vol. 7, pp. 95-100).*

Brown, J. 1969. *Ionic Concentration Gradients in Permafrost, Barrow, Alaska*. Corps of Engineers, U.S. Army, Cold Regions Research and Engineering Laboratory.

CALM. 2024. "The Circumpolar Active Layer Monitoring Network-CALM V (2019-2024): Long-term Observations on the Climate-Active Layer-Permafrost System.George Washington University." https://www.gwu.edu/~calm/.

Christ, M., Y. C. Kim, and J. B. Park. 2009. "The influence of temperature and cycles on acoustic and mechanical properties of frozen soils." *KSCE Journal of Civil Engineering*, 13 (3): 153–159. https://doi.org/10.1007/s12205-009-0153-1.

Chuvilin, E. M., B. A. Bukhanov, A. Z. Mukhametdinova, E. S. Grechishcheva, N. S. Sokolova, A. G. Alekseev, and V. A. Istomin. 2022. "Freezing point and unfrozen water contents of permafrost soils: Estimation by the water potential method." *Cold Regions Science and Technology*, 196: 103488. https://doi.org/10.1016/j.coldregions.2022.103488.

Dall'Amico, M., S. Endrizzi, S. Gruber, and R. Rigon. 2011. "A robust and energy-conserving model of freezing variably-saturated soil." *The Cryosphere*, 5 (2): 469–484. Copernicus GmbH. https://doi.org/10.5194/tc-5-469-2011.

Dyer, A. J. 1974. "A review of flux-profile relationships." *Boundary-Layer Meteorology*, 7 (3): 363–372. https://doi.org/10.1007/BF00240838.

Farley, M., E. Lathrop, S. Dillard, R. Crumley, C. Trotter, E. Gasarch, D. Yang, B. Bolton, C. J. Abolt, X. Huang, and K. E. Bennett. 2026. "Soil Texture and Organic Matter from Teller Field Site and Barrow Environmental Observatory, Alaska, 2024." Next-Generation Ecosystem Experiments (NGEE) Arctic, ESS-DIVE repository. doi:10.15485/2587411.

Farouki, O. 1981. *Thermal Properties of Soils*. U.S. Army Corps of Engineers, Cold Regions Research and Engineering Laboratory.

Fushiki, T. 2011. "Estimation of prediction error by using K-fold cross-validation." *Statistics and Computing*, 21 (2): 137–146. https://doi.org/10.1007/s11222-009-9153-8.

van Genuchten, M. Th. 1980. "A closed-form equation for predicting the hydraulic conductivity of unsaturated soils." *Soil Science Society of America Journal*, 44 (5): 892–898. https://doi.org/10.2136/sssaj1980.03615995004400050002x.

van Genuchten, M. Th., and J. C. Parker. 1984. "Boundary conditions for displacement experiments through short laboratory soil columns." *Soil Science Society of America Journal*, 48 (4): 703–708. https://doi.org/10.2136/sssaj1984.03615995004800040002x.

Hansson, K., J. Šimůnek, M. Mizoguchi, L.-C. Lundin, and M. Th. van Genuchten. 2004. "Water flow and heat transport in frozen soil: numerical solution and freeze–thaw applications." *Vadose Zone Journal*, 3 (2): 693–704. https://doi.org/10.2113/3.2.693.

Hersbach, H., B. Bell, P. Berrisford, S. Hirahara, A. Horányi, J. Muñoz-Sabater, J. Nicolas, C. Peubey, R. Radu, D. Schepers, A. Simmons, C. Soci, S. Abdalla, X. Abellan, G. Balsamo, P. Bechtold, G. Biavati, J. Bidlot, M. Bonavita, G. De Chiara, P. Dahlgren, D. Dee, M. Diamantakis, R. Dragani, J. Flemming, R. Forbes, M. Fuentes, A. Geer, L. Haimberger, S. Healy, R. J. Hogan, E. Hólm, M. Janisková, S. Keeley, P. Laloyaux, P. Lopez, C. Lupu, G. Radnoti, P. de Rosnay, I. Rozum, F. Vamborg, S. Villaume, and J.-N. Thépaut. 2020. "The ERA5 global reanalysis." *Quarterly Journal of the Royal Meteorological Society*, 146 (730): 1999–2049. https://doi.org/10.1002/qj.3803.

Hinkel, K. M., and F. E. Nelson. 2003. "Spatial and temporal patterns of active layer thickness at Circumpolar Active Layer Monitoring (CALM) sites in northern Alaska, 1995–2000." *Journal of Geophysical Research: Atmospheres*, 108 (D2). https://doi.org/10.1029/2001JD000927.

Johansen, O. 1977. "Thermal Conductivity of Soils." 322.

Kim, S., H.-J. Choi, S. Park, and Y. Kim. 2025. "Predicting the freezing characteristics of organic soils using laboratory experiments and machine learning models." *Applied Sciences*, 15 (19): 10314. Multidisciplinary Digital Publishing Institute. https://doi.org/10.3390/app151910314.

Kokelj, S. V., and M. T. Jorgenson. 2013. "Advances in thermokarst research." *Permafrost and Periglacial Processes*, 24 (2): 108–119. https://doi.org/10.1002/ppp.1779.

Koopmans, R. W. R., and R. D. Miller. 1966. "Soil freezing and soil water characteristic curves." *Soil Science Society of America Journal*, 30 (6): 680–685. https://doi.org/10.2136/sssaj1966.03615995003000060011x.

Kurylyk, B. L., and K. Watanabe. 2013. "The mathematical representation of freezing and thawing processes in variably-saturated, non-deformable soils." *Advances in Water Resources*, 60: 160–177. https://doi.org/10.1016/j.advwatres.2013.07.016.

Lara, M. J., I. Nitze, G. Grosse, and A. D. McGuire. 2018. "Tundra landform and vegetation productivity trend maps for the Arctic Coastal Plain of northern Alaska." *Scientific Data*, 5 (1): 180058. Nature Publishing Group. https://doi.org/10.1038/sdata.2018.58.

Lawrence, D., R. Fisher, C. Koven, S. Swenson, and M. Vertenstein. 2020. "Technical description of version 5.0 of the Community Land Model (CLM)." National Center for Atmospheric Research.

Lawrence, D. M., and A. G. Slater. 2008. "Incorporating organic soil into a global climate model." *Climate Dynamics*, 30 (2): 145–160. https://doi.org/10.1007/s00382-007-0278-1.

Li, K.-Q., and H.-L. He. 2024. "Towards an improved prediction of soil-freezing characteristic curve based on extreme gradient boosting model." *Geoscience Frontiers*, 15 (6): 101898. https://doi.org/10.1016/j.gsf.2024.101898.

Liljedahl, A. K., J. Boike, R. P. Daanen, A. N. Fedorov, G. V. Frost, G. Grosse, L. D. Hinzman, Y. Iijma, J. C. Jorgenson, N. Matveyeva, M. Necsoiu, M. K. Raynolds, V. E. Romanovsky, J. Schulla, K. D. Tape, D. A. Walker, C. J. Wilson, H. Yabuki, and D. Zona. 2016. "Pan-Arctic ice-wedge degradation in warming permafrost and its influence on tundra hydrology." *Nature Geoscience*, 9 (4): 312–318. Nature Publishing Group. https://doi.org/10.1038/ngeo2674.

Liu, M., P. Zhuang, and R. Fuentes. 2026. "Data-driven ANN model for estimating unfrozen water content in the thermo-hydraulic simulation of frozen soils." *Computers and Geotechnics*, 192: 107846. https://doi.org/10.1016/j.compgeo.2025.107846.

Meng, X., J. Zhou, C. Wei, K. Zhang, Z. Shen, and Z. Yang. 2020. "Effects of salinity on soil freezing temperature and unfrozen water content." *Rock and Soil Mechanics*, 41 (3): 952–960. https://doi.org/10.16285/j.rsm.2019.0617.

Millington, R. J., and J. P. Quirk. 1961. "Permeability of porous solids." *Transactions of the Faraday Society*, 57 (0): 1200–1207. The Royal Society of Chemistry. https://doi.org/10.1039/TF9615701200.

Monin, A. S., and A. M. Obukhov. 1954. "Basic laws of turbulent mixing in the surface layer of the atmosphere." *Contrib. Geophys. Inst. Acad. Sci. USSR*, 151 (163).

Mualem, Y. 1976. "A new model for predicting the hydraulic conductivity of unsaturated porous media." *Water resources research*, 12 (3): 513–522. https://doi.org/10.1029/WR012i003p00513.

Nemes, A., M. G. Schaap, F. J. Leij, and J. H. M. Wösten. 2001. "Description of the unsaturated soil hydraulic database UNSODA version 2.0." *Journal of Hydrology*, 251 (3): 151–162. https://doi.org/10.1016/S0022-1694(01)00465-6.

Nicolsky, D., and T. Wright. 2024. "Understand and forecast long-term variations of in-situ geophysical and geomechanical characteristics of degrading permafrost in the Arctic - continuously observed ground temperatures, Utqiagvik, Alaska, 2022-2023." Arctic Data Center.
Nicolsky, D., and T. Wright. 2025. "Understand and forecast long-term variations of in-situ geophysical and geomechanical characteristics of degrading permafrost in the Arctic - continuously observed ground temperatures, Utqiagvik, Alaska, 2024-2025." Arctic Data Center.
Park, S., Y. Choe, H. Choi, and K. Pham. 2025. "Machine learning-based pseudo-continuous pedotransfer function for predicting soil freezing characteristic curve." *Geoderma*, 453: 117145. https://doi.org/10.1016/j.geoderma.2024.117145.
Pitzer, K. S. 1975. "Thermodynamics of electrolytes. V. effects of higher-order electrostatic terms." *Journal of Solution Chemistry*, 4 (3): 249–265. https://doi.org/10.1007/BF00646562.
Ren, J., X. Fan, X. Yu, S. Vanapalli, and S. Zhang. 2023. "Use of an artificial neural network model for estimation of unfrozen water content in frozen soils." *Canadian Geotechnical Journal*, 60 (8): 1234–1248. https://doi.org/10.1139/cgj-2022-0035.
Romanovsky, V., A. Kolodov, N. Hasson, D. Nicolsky, and T. Wright. 2019. "Thermal State of Permafrost in North America - continuously observed ground temperatures, 2016-2017." Arctic Data Center. doi:10.18739/A24J09X6N.
Shur, Y. L., and M. T. Jorgenson. 2007. "Patterns of permafrost formation and degradation in relation to climate and ecosystems." *Permafrost and Periglacial Processes*, 18 (1): 7–19. https://doi.org/10.1002/ppp.582.
Spencer, R. J., N. Møller, and J. H. Weare. 1990. "The prediction of mineral solubilities in natural waters: A chemical equilibrium model for the Na-K-Ca-Mg-Cl-SO4-H2O system at temperatures below 25°C." *Geochimica et Cosmochimica Acta*, 54 (3): 575–590. https://doi.org/10.1016/0016-7037(90)90354-N.
Tourei, A., X. Ji, G. Rocha dos Santos, R. Czarny, S. Rybakov, Z. Wang, M. Hallissey, E. R. Martin, M. Xiao, T. Zhu, D. Nicolsky, and A. Jensen. 2024. "Mapping permafrost variability and degradation using seismic surface waves, electrical resistivity, and temperature sensing: a case study in Arctic Alaska." *Journal of Geophysical Research: Earth Surface*, 129 (3): e2023JF007352. https://doi.org/10.1029/2023JF007352.
Walvoord, M. A., and B. L. Kurylyk. 2016. "Hydrologic impacts of thawing permafrost—A review." *Vadose Zone Journal*, 15 (6): vzj2016.01.0010. https://doi.org/10.2136/vzj2016.01.0010.
Wan, X., F. Gong, M. Qu, E. Qiu, and C. Zhong. 2019. "Experimental study of the salt transfer in a cold sodium sulfate soil." *KSCE Journal of Civil Engineering*, 23 (4): 1573–1585. https://doi.org/10.1007/s12205-019-0905-5.
Wang, Y., and L. Hu. 2023. "A theoretical model of soil freezing characteristic curve considering the freezing of adsorbed water and capillary water." *Water Resources Research*, 59 (7): e2023WR034662. https://doi.org/10.1029/2023WR034662.
Wang, Y., and N. Lu. 2026. "Defining the soil freezing characteristic curve directly from the generalized soil water characteristic curve." *Journal of Geotechnical and Geoenvironmental Engineering*, 152 (4): 04026015. American Society of Civil Engineers. https://doi.org/10.1061/JGGEFK.GTENG-14335.
Wang, Z., M. Xiao, M. Bray, D. Nicolsky, and X. Ji. 2026. "Creep deformation and long-term strength of ice-rich permafrost in Northern Alaska." *Journal of Geotechnical and Geoenvironmental Engineering*, 152 (1): 04025161. American Society of Civil Engineers. https://doi.org/10.1061/JGGEFK.GTENG-13324.
Watanabe, K., and T. Wake. 2009. "Measurement of unfrozen water content and relative permittivity of frozen unsaturated soil using NMR and TDR." *Cold Regions Science and Technology*, 59 (1): 34–41. https://doi.org/10.1016/j.coldregions.2009.05.011.
Westermann, S., T. Ingeman-Nielsen, J. Scheer, K. Aalstad, J. Aga, N. Chaudhary, B. Etzelmüller, S. Filhol, A. Kääb, C. Renette, L. S. Schmidt, T. V. Schuler, R. B. Zweigel, L. Martin, S. Morard, M. Ben-Asher, M. Angelopoulos, J. Boike, B. Groenke, F. Miesner, J. Nitzbon, P. Overduin, S. M. Stuenzi, and M. Langer. 2023. "The CryoGrid community model (version 1.0) – a multi-physics toolbox for climate-driven simulations in the terrestrial cryosphere." *Geoscientific Model Development*, 16 (9): 2607–2647. Copernicus GmbH. https://doi.org/10.5194/gmd-16-2607-2023.
Westermann, S., M. Langer, J. Boike, M. Heikenfeld, M. Peter, B. Etzelmüller, and G. Krinner. 2016. "Simulating the thermal regime and thaw processes of ice-rich permafrost ground with the land-surface model CryoGrid 3." *Geoscientific Model Development*, 9 (2): 523–546. Copernicus GmbH. https://doi.org/10.5194/gmd-9-523-2016.
Wu, Y., Y. Wang, and L. Hu. 2023. "A theoretical model of the soil freezing characteristic curve for saline soil." *Journal of Hydrology*, 622: 129639. https://doi.org/10.1016/j.jhydrol.2023.129639.
Zhang, J., Y. Lai, M. Zhang, Z. You, S. Li, and R. Bai. 2024. "Study on the coupling mechanism of water-heat-vapor-salt-mechanics in unsaturated freezing sulfate saline soil." *Computers and Geotechnics*, 169: 106232. https://doi.org/10.1016/j.compgeo.2024.106232.

Zhou, J., X. Meng, C. Wei, and W. Pei. 2020. "Unified soil freezing characteristic for variably-saturated saline soils." *Water Resources Research*, 56 (7): e2019WR026648. https://doi.org/10.1029/2019WR026648.
Zhou, J., C. Wei, Y. Lai, H. Wei, and H. Tian. 2018. "Application of the generalized clapeyron equation to freezing point depression and unfrozen water content." *Water Resources Research*, 54 (11): 9412–9431. https://doi.org/10.1029/2018WR023221.

Department of Civil and Environmental Engineering, The Pennsylvania State University, University Park, PA 16802, United States of America

Email address: xxw5360@psu.edu

Email address: mzx102@psu.edu